Materials Advances

ROYAL SOCIETY OF CHEMISTRY

PAPER

View Article Online
View Journal

Cite this: DOI: 10.1039/d5ma01038a

Development of organic–inorganic hybrid coatings with silica nanoparticles, biopolymers, and clay for onion seeds: a multifunctional strategy for controlling white rot

Lorena Alves de Melo Bessa, *[a] Franciely Junia Alves de Camargos,[a] Amanda Maria de Oliveira,[a] Celly Mieko Shinohara Izumi, [b] Everaldo Antônio Lopes, [a] Eduardo Alves, [c] Eduardo S. G. Mizubuti [d] and Jairo Tronto [a]

White rot, caused by *Stromatinia cepivora*, remains one of the most challenging soil-borne diseases affecting onion crops due to the long-term persistence of sclerotia and the limited effectiveness of conventional fungicide treatments. Silicon has been reported to contribute to plant defense and disease suppression, and when incorporated into coatings, it can contribute to the formation of a mechanical barrier against external agents, making its action interesting in conjunction with low concentrations of commercially used fungicidal active ingredients. Hybrid coatings containing fungicidal active ingredients and SiO_2 nanoparticles were developed and evaluated for their effects on onion seed germination and inhibition of *S. cepivora* mycelial growth. The coating containing SiO_2 nanoparticles and fungicidal active ingredients (CS5-TR and CS5-TE) showed 100% inhibition of mycelial growth under *in vitro* contact conditions. Raman and FTIR-ATR spectroscopy techniques confirmed the presence of CMC and LAPONITE® RD precursors in the coatings, as well as slight shifts and a reduction in band intensity when combined with fungicidal actives and SiO_2 NPs. X-ray diffraction (XRD) combined with scanning electron microscopy (SEM) confirmed the presence of SiO_2 NPs in the hybrid coatings, amorphizing the (001) peak, characteristic of the presence of LAPONITE® RD. This suggests structural reorganization of the polymer–clay–silica matrix after the addition of SiO_2 in the interlayer spaces of the clay, consistent with a reduction in stacking order and changes in the coating morphology. TG-DSC thermal analysis showed an event around 300 °C, mainly attributed to the degradation of the organic matrix and the loss of bound water. Energy-dispersive X-ray spectroscopy (EDS) confirmed the presence of O, Na, Si, Mg, and F in the coatings, suggesting the formation of SiO_2 nanoparticle agglomerates on the surface during the drying process. The use of SiO_2 NPs and fungicidal active ingredients incorporated into the synthesis of organic–inorganic hybrid materials demonstrated enhanced antifungal performance, highlighting the potential of hybrid coatings as a multifunctional strategy for controlling white rot, although their release kinetics, permeability, fungal cell damage, and soil/greenhouse performance still need to be investigated.

Received 9th September 2025,
Accepted 26th May 2026

DOI: 10.1039/d5ma01038a

rsc.li/materials-advances

1. Introduction

Organic–inorganic hybrid materials have been widely used as carriers of substances in various segments due to the combination of the functionality and flexibility of the organic polymer matrix with the characteristics of inorganic particles, such as optical, magnetic, and electrical properties, as well as thermal stability and mechanical and chemical resistance.[1] Their primary use in agriculture is the carrier system of nutrients and inputs for crop development and treatment.

The incorporation of agrochemical actives into organic–inorganic hybrid materials can significantly reduce the amount of agrochemicals applied to crops. In contrast, these materials coat plant structures, such as seeds, producing a hybrid coating with high swelling power and protective characteristics.[2–4]

In addition to reducing the high volume of agrochemicals used in agriculture, the use of substances and materials that present new application possibilities and act as fungicides,

[a] Instituto de Ciências Exatas e Tecnológicas, Universidade Federal de Viçosa, Campus Rio Paranaíba, CEP 38810-000, Rio Paranaíba, MG, Brazil. E-mail: jairotronto@ufv.br
[b] Departamento de Química, Instituto de Ciências Exatas, Universidade Federal de Juiz de Fora, Campus Univeritário, CEP 36036-900, Juiz de Fora, MG, Brazil. E-mail: celly.izumi@ufjf.br
[c] Departamento de Fitopatologia, Universidade Federal de Lavras, Lavras, CEP 37200-900, MG, Brazil. E-mail: ealves@ufla.br
[d] Departamento de Fitopatologia, Universidade Federal de Viçosa, Campus Viçosa, CEP 36570-900, Viçosa, MG, Brazil. E-mail: mizubuti@ufv.br

insecticides, herbicides, and fertilizers has been encouraged. In this sense, silicon and its derivatives have been investigated due to their porosity and adsorbent capacity for molecules in liquid and gas phases.[5,6]

Found in the soil in the form of silicon oxides, this element is related to final productivity, due to the improvement of morphological and physiological aspects in the plant cycle. Silicon forms a protective layer on the walls of the cellular transpiration organs of plants, acting to reduce evapotranspiration, which favors development in periods of drought and low water supply. In addition, the double layer of silica-cuticle and silica-cellulose formed acts as a mechanical barrier to the entry of external agents. Due to this characteristic, silicon has antifungal activity that has been studied for its use in crops affected by these microorganisms.[7,8] Among them, white rot caused by the fungus *Stromatinia cepivora* (Berk.) Whetzel affects crops of the Alliaceae family, mainly garlic (*Allium sativum* L.) and onion (*Allium cepa* L.). The sclerotia, cylindrical structures produced by the fungus, germinate in the soil from the release of exudates by the roots of the Alliaceae, such as allicin and diallyl sulfur. Hyphae then branch out and infect the host plants approximately 14 days after the germination of the sclerotia. Some of the characteristic symptoms of white rot disease include yellowing and wilting of the aerial part and decomposition of roots and bulbs.[9,10] Unlike previous studies that have separately explored polymer–clay seed coatings, silica-based antifungal materials, or fungicide delivery systems, this study investigates a hybrid organic–inorganic coating specifically designed for onion seeds and white rot control.[10] The proposed system combines sodium carboxymethyl cellulose, LAPONITE® RD, SiO_2 nanoparticles (SiO_2 NPs), and triazole fungicides in a single thin coating. Its main contribution is not the isolated use of these components, but the demonstration that their combination, particularly the incorporation of SiO_2 into triazole-containing coatings, is associated with markedly improved antifungal performance against *Stromatinia cepivora*.[11–14] Specifically, the work has the following objectives: (i) to prepare organic–inorganic hybrid coatings containing LAPONITE® RD clay, a sodium carboxymethyl cellulose biopolymer, fungicidal actives (kresoxim-methyl, dimoxtrobin, tebuconazole, triadimenol or boscalid) and SiO_2; (ii) to investigate the interaction between SiO_2, fungicides and hybrid coatings using Fourier transform infrared-attenuated total reflection (FTIR-ATR) spectroscopy, Raman spectroscopy, scanning electron microscopy (SEM), thermogravimetric analysis (TG-DTG-DSC), and X-ray diffraction (XRD); and (iii) to evaluate the inhibitory effect of the produced organic–inorganic hybrid materials on the growth of *S. cepivora*.

2. Experimental section

2.1 Reagents

The following reagents were used to prepare the organic–inorganic hybrid materials: LAPONITE® RD (LAP) was supplied by Buntech (São Paulo, Brazil); sodium carboxymethyl cellulose (CMC), tebuconazole (TB), triadimenol (TD), boscalid (BC), kresoxim-methyl (CM), dimoxtrobin (DM), and silicon dioxide nanoparticles (SiO_2 NPs) were produced by Merck (Darmstadt, Germany). Deionized water was obtained using a Milli-Q water purification system (Millipore, France).

2.2 Preparation of organic–inorganic hybrid materials for coating onion seeds

All solutions and dispersions were prepared under magnetic stirring to ensure homogeneity. The dispersions containing LAPONITE® RD in their composition were kept on a hot plate under stirring at 80 °C until complete solubilization and exfoliation of the clay tactoids.

2.3 Structural characterization of organic–inorganic hybrid materials

2.3.1 X-ray diffraction (XRD). A Shimadzu model XRD-6000 X-ray diffractometer was used for analysis. A graphite crystal monochromator was used to select Cu-Kα1 radiation with a wavelength of λ = 1.5406 Å. The source's electrical current and potential were 30 mA and 30 kV, respectively. The diffractograms were collected between (2θ) 4° and 70°, with a step of 1.0° per minute.

2.3.2 Molecular absorption spectrophotometry in the infrared region with Fourier transform and attenuated total reflectance (FTIR-ATR) accessory. A Jasco model FTIR 4100 spectrophotometer with an attached ATR accessory was used. The spectra obtained by the analysis resulted from 256 scans with a resolution of 4 cm^{-1} and a wave number range of 4000 to 400 cm^{-1}.

2.3.3 Vibrational Raman spectroscopy. The spectra were recorded on an FT-Raman spectrometer (model RFS100/S, Bruker Optics) using an Nd: YAG laser with excitation at 1064 nm. The power used was 100 mW, with a resolution of 4 cm^{-1} and 1024 scans.

2.3.4 Thermogravimetric analysis and differential scanning calorimetry (TGA-DSC). Thermogravimetric analyses were carried out using a 28 Netzsch STA 409 PC – Luxx thermobalance for simultaneous TG-DSC analysis coupled to a Netzsch mass spectrometer (model QMS 403 C – Aeölos) for detecting gases released from the sample. Approximately 5 mg of the sample was placed in an alumina crucible and heated at 10 °C min^{-1} in a synthetic air flow (80% N_2 and 20% O_2) of 100 cm^3 min^{-1}, from 30 °C to 1000 °C.

2.3.5 Scanning electron microscopy (SEM). For scanning electron microscopy analyses, a LEO EVO 40 XVP scanning electron microscope (SEM) was used, equipped with Bruker X-ray microanalysis systems (Quantax EDS and Espirit Software) and a Gatan cryotransfer and cryo-observation systems (Alto 1000).

2.4 Coating of onion seeds to evaluate the sprouting rate

Seventeen different coatings were prepared for onion seeds (*Allium cepa*) from a combination of sodium carboxymethyl cellulose (CMC) polymer, LAPONITE® synthetic clay, and 20 nm SiO_2 NPs. The coatings were prepared by stirring in volumetric flasks under a magnetic stirrer and heating at 50 °C for 4 hours until complete solubilization, and stored under refrigeration for the germination test. The onion seeds (Allium cepa L.) used in the experiment were provided by Embrapa Hortaliças, lot BRS

Table 1 Composition of the coatings

Coatings	CMC (wt%)	LAP® RD (wt%)	SiO_2 (wt%)
CS1	99.0	0.0	1.0
CS2	97.5	0.0	2.5
CS3	95.0	0.0	5.0
CS4	92.5	0.0	7.5
CS5	90.0	0.0	10.0
LS1	0.0	99.0	1.0
LS2	0.0	97.5	2.5
LS3	0.0	95.0	5.0
LS4	0.0	92.5	7.5
LS5	0.0	90.0	10.0
CLS1	49.5	49.5	1.0
CLS2	48.8	48.8	2.5
CLS3	47.5	47.5	5.0
CLS4	46.3	46.3	7.5
CLS5	45.0	45.0	10.0
L1-LAP	0.0	100.0	0.0
L1-CMC	100.0	0.0	0.0

CMC (wt%): mass percentage of CMC; LAPONITE® RD (wt%): mass percentage of LAPONITE® RD clay; SiO_2 (wt%): mass percentage of SiO_2 NPs

Belatriz 239. The onion seeds were immersed in 20 mL of each coating (Table 1) for 30 minutes. The gerboxes were previously sterilized in 70° GL ethyl alcohol, and the germination paper was sterilized in an oven at 105 °C for 2 hours. Planting was carried out in gerboxes with germination paper, containing 20 seeds arranged in five rows of four seeds each. The boxes were kept in a BOD chamber with a 12 hour photoperiod at 25 °C. The germinated seeds were counted between the 6th and 12th days after planting. The following variables were evaluated: germination percentage, germination speed (VG), germination speed index (IVG), and average germination time (TMG). The germination percentage (G) was calculated using the formula $G = (N/A) \times 100$, where N represents the number of germinated seeds and A, the total number of seeds in the sample. The germination speed index (GSI) was given by the formula $GSI = \sum(n_i/t_i)$, where n_i is the number of germinated seeds at time "i" and t_i is the time in days from the beginning of the experiment. The average germination time (AGT) was calculated using the formula $AGT = ((\Sigma n_i t_i)/\Sigma n_i)$, where n_i represents the number of germinated seeds daily and t_i represents the incubation time. The average germination speed (AGS) is calculated using the formula $AGS = 1/t$, where t represents the average germination time. The coatings that presented the best results were selected for the next stage of the experiment. Due to the exploratory nature of the germination screening and the use of a single germination box per treatment, the results were analyzed using multivariate analysis (PCA) rather than inferential statistical comparisons. This approach allows identifying treatments with the best overall germination performance while avoiding pseudoreplication.

2.5 Mycelial growth inhibition (MGI) for the evaluation of onion seed coatings

For the mycelial growth inhibition study, solutions of the active fungicides triadimenol at 62 mg L^{-1}, tebuconazole at 36 mg L^{-1}, and boscalid at 4.6 mg L^{-1} were prepared. These solutions were used as a basis for synthesizing the coatings. The experiment was conducted in a completely randomized design (CRD) with four replications. One replication consisted of a plate containing a mycelial disc of *S. cepivora* equidistant from three pieces of dry coatings of the hybrid materials in approximately 15 mL of PDA medium – potato dextrose agar. The positive control was performed with the active ingredient iprodione (Magic®, 500 gL^{-1}), traditionally used in garlic and onion cultivation, to compare its inhibitory effect on mycelial growth with that of the synthesized coatings. The negative controls were composed of PDA media without fungicides and a *S. cepivora* mycelial disc (CNM) to evaluate possible contamination of the medium; PDA culture medium with a mycelial disc (CNMB) to evaluate fungal growth; PDA culture medium containing three pieces of dried coating films. Two repetitions were performed (CN1 and CN2) to observe possible contamination in the dried coating films.

After preparing the plates, they were kept at 17 °C with a 12 hour photoperiod. The mycelial growth of the fungus was monitored daily. The experiment was terminated once the control treatment reached full plate colonization, which defined the endpoint of the assay under the growth conditions used for *S. cepivora*. The data on mycelial growth inhibition were evaluated for statistical differences using the non-parametric Kruskal–Wallis test, followed by Dunn's post-hoc test for multiple comparisons. Differences were considered statistically significant at $p < 0.05$.

3. Results and discussion

3.1 Results of the coating of onion seeds for evaluation of the sprouting rate

During the 15-day evaluation period, differences in germination variables were observed among treatments. Their overall behavior was explored using principal component analysis (PCA). Fig. S3 presents the principal component analysis (PCA) of the germination parameters for the coated seeds. Coatings 15 (CS4), 16 (CS5), 12 (CS1), and 13 (CS2), all formulated with the CMC polymer and SiO_2, showed higher values for the germination percentage (G) and germination speed index (GSI). Coatings 17 (L1-Lap) and 18 (L1-CMC) also showed relevant values for G and GSI, even in the absence of SiO_2. Notably, coating 6 (LS5), composed of 90% LAP (wt%) and 10% SiO_2 (wt%), showed the highest IVG among all samples. Regarding the second principal component (PC2), coating 14 (CS3) obtained the highest score, demonstrating a strong correlation with the mean germination time (MGT). Descriptive statistical analysis of germination parameters (Table S1) indicated an average germination rate of 87.6% among the evaluated treatments. The mean germination time (TMG) showed low variability (CV ≈ 9%), suggesting similar germination dynamics among most coatings. The germination speed index (IVG) presented the highest coefficient of variation (16%), indicating greater sensitivity to differences among the hybrid coatings. Overall, the treatments containing SiO_2 NPs and fungicides tended to cluster in the region associated with higher germination speed and lower mean germination time, indicating that the presence of SiO_2 does not negatively affect seed germination

performance. The observed germination rates are consistent with the multifunctional role of hybrid coatings. The hydrophilic polymeric matrix (CMC or LAP) enables controlled water absorption on the seed surface, promoting uniform hydration and activation of metabolic processes without excessive swelling. Meanwhile, SiO_2 NPs introduce micro- and nanoscale porosity and surface roughness, enhancing water retention and gas permeability, which facilitates oxygen diffusion and respiratory activity during early germination.

Together, these effects accelerate radicle emergence, leading to higher germination percentages and faster germination rates. Under the exploratory screening conditions used here, SiO_2-containing coatings did not show an apparent detrimental effect on germination parameters. However, because the germination assay was performed with a single germination box per treatment, these results should be interpreted qualitatively and require confirmation in replicated assays.

3.2 Results of the mycelial growth inhibition (MGI)

The presence of SiO_2 contributes to the formation of a nanostructured coating that increases surface roughness and mechanical discontinuity, which may hinder fungal adhesion and hyphal penetration. Simultaneously, nanoparticles may promote a more homogeneous distribution of fungicidal actives in the polymeric matrix, potentially decreasing phase separation and increasing the contact area between the active ingredients and the fungal mycelium. Among the fungicidal agents evaluated (Table 2), the BTE coating containing tebuconazole showed the greatest inhibition of mycelial growth of *S. cepivora* (74.55%), highlighting the intrinsic efficacy of this compound. When associated with SiO_2 NPs, the active ingredients tebuconazole and triadimenol, in the CS5-TE and CS5-TR coatings, achieved complete inhibitory effects on mycelial growth in the treated plates (Fig. S4). In paired comparisons, inhibition increased from 27.73% for BTR to 100.00% for CS5-TR and from 74.55% for BTE to 100.00% for CS5-TE. In contrast, the boscalid-containing formulation showed no improvement after SiO_2 incorporation, indicating that the effect of the nanostructured matrix depends on the active ingredient and coating composition. The incorporation of SiO_2 NPs affected mycelial growth inhibition in a formulation-dependent manner. Enhanced inhibition was observed for several active ingredients, particularly for triazole-containing coatings. Triazoles inhibit ergosterol biosynthesis, compromising the integrity of the fungal cell membrane, while the nanostructured matrix reinforced with SiO_2 may be associated with reduced fungal growth, although the underlying mechanisms (*e.g.*, permeability or release kinetics) were not directly evaluated in this study. A possible interpretation is that the hybrid coating architecture may favor sustained contact between the fungicidal actives and the pathogen, thereby contributing to the stronger inhibitory response observed for the silica-containing triazole coatings.[15] Antifungal performance was evaluated under *in vitro* conditions; further validation under soil conditions is necessary before practical application.

Table 2 Percentage of mycelial growth inhibition (MGI)

Treatment	Fungicide	Colony area (cm^2)	MGI[a] (%)
BR	—	25.00	57.14 d
BB	Boscalid	27.76	52.42 e
BCM	Cresoxim-methyl	30.48	47.79 f
BDM	Dimoxistrobin	48.06	17.65 i
BTR	Triadimenol	42.18	27.73 h
BTE	Tebuconazole	14.86	74.55 c
CS5-BB	Boscalid	33.90	41.91 g
CS5-CM	Cresoxim-methyl	7.31	87.48 b
CS5-DM	Dimoxistrobin	26.71	54.23 e
CS5-TR	Triadimenol	0.00	100.00 a
CS5-TE	Tebuconazole	0.00	100.00 a
CN1-CN3	—	0.00	100.00
CN2	—	100.00	0.00
CP (Control)	Iprodione	13.60	—

[a] Different letters indicate significant differences among treatments according to Dunn's test ($p < 0.05$) after Kruskal–Wallis analysis.

3.3 Characterization of organic–inorganic hybrid materials

3.3.1 X-ray diffraction analysis (XRD). In the diffractograms of pure LAPONITE® RD clay, an initial broad peak is observed, referring to the diffraction of the (001) atomic plane, in the 2θ region equal to 6.78°. The width of the peak is justified by the low structural organization in the stacking direction of the LAPONITE® RD lamellae, which is directly related to the size of the clay nanoparticles and the presence of water molecules surrounding the cations present in the interlamellar domain.[16–18] This structural disorder is particularly relevant for the formation of hybrid coatings, as it facilitates intercalation and interaction with polymer chains and nanoparticles. The disappearance of the (001) peak of LAPONITE® RD after the incorporation of SiO_2 NPs (Fig. 1A-(f), (g) and B-(f), (g)) indicates disruption of the original clay stacking/interlayer organization after SiO_2 incorporation. When considered together with the SEM cross-sectional images, this structural change is consistent with the formation of thinner and more flexible dried coating films, which exhibited the strongest antifungal performance. The diffractograms of the polymer sodium carboxymethyl cellulose (P.A.) show an intense peak characteristic of the polymer in the 2θ region equal to 20°.[19] The biopolymer has a predominantly amorphous character and a reduced degree of crystallinity with the formation of gels, which may cause the disappearance of its crystalline peaks. This may be related to the increase in the distance of the polymer atoms after synthesis, with the incorporation of other atoms in the CMC crystal lattice.[20] The three peaks evidenced in the 2θ region between 35° and 65° in the diffractograms of Fig. 1A-((c), (d), (e), (f) and (g)) and (B)-((c), (d), (e), (f) and (g)), are characteristic of the presence of metallic aluminium from the equipment sample holder.[21] The other peaks characteristic of the precursor materials exhibited smaller and broader peaks, which may be related to the dilution effect of the polymer matrix and the interaction between the components.

This occurrence can be illustrated by the reduction of the peaks associated with LAPONITE® RD, sodium carboxymethyl cellulose, and active ingredients triadimenol and tebuconazole in the diffractograms of the synthesized materials, when compared to the precursors in their pure P.A. form. In the diffractograms of

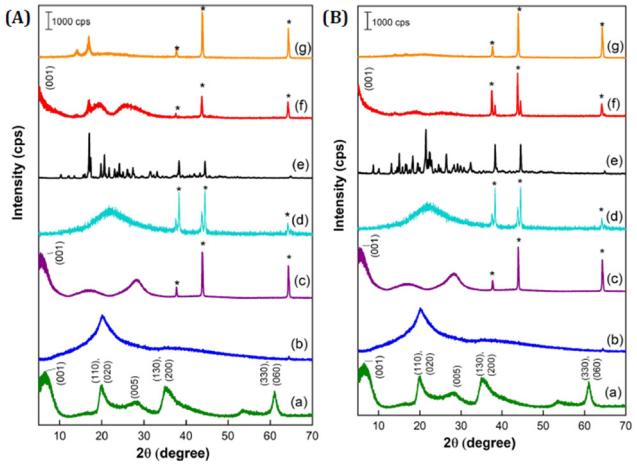

Fig. 1 Diffractograms of (A) - (a) LAP P.A.; (b) CMC P.A.; (c) coating composed of 2% CMC and 2% LAP; (d) SiO_2 NPs P.A.; (e) TB P.A.; (f) coating composed of 2% CMC, 2% LAP and 36 mg L^{-1} TB – (BTE); (g) coating composed of 2% CMC, 2% LAP, 36 mg L^{-1} TB, and 10% SiO_2 NPs – (CS5-TE) and for (B) – (a) LAP P.A.; (b) CMC P.A.; (c) coating composed of 2% CMC and 2% LAP; (d) SiO_2 NPs P.A.; (e) TD P.A.; (f) coating composed of 2% CMC, 2% LAP, and 62 mg L^{-1} TD – (BTR); (g) coating composed of 2% CMC, 2% LAP, 62 mg L^{-1} TD, and 10% SiO_2 NPs – (CS5-TR).

the SiO_2 NPs, shown in Fig. 1A and B-(d), a broad diffraction peak is observed in the 2θ region between 15° and 30°, referring to the diffraction of the atomic plane characteristic of amorphous silica, in addition to the crystalline peaks of the aluminium sample port, previously described.[22,23]

In the diffractograms of Fig. 1A and B-(e), the crystalline peaks of tebuconazole and triadimenol are shown, respectively. Since both are triazole actives, with similar molecular compositions, they present numerous diffraction peaks in the same 2θ region, between 5° and 45°. The absence of diffraction peaks of the fungicides tebuconazole and triadimenol in the diffractograms of the synthesized materials, in Fig. 1A-(f) and (g) and B-(f) and (g), can be justified by the interaction with the other precursors, causing the amorphization of the material.[24,25] In the diffractograms of Fig. 1A and B-(g), which show, respectively, materials CS5-TR and CS5-TE, the disappearance of the (001) peak, characteristic of the presence of LAPONITE® RD clay, is observed, suggesting disruption or expansion of the clay interlayer structure after SiO_2 incorporation.[26] This suggests that the incorporation of SiO_2 NPs promotes the amorphization of the polymeric matrix by interfering with crystalline packing and increasing the disordered interfacial fraction, which may indicate increased structural disorder. However, no direct measurements of permeability or fungicide release kinetics were performed.

3.3.2 Analysis by molecular absorption spectrophotometry in the infrared region with Fourier transform and attenuated total reflectance accessory (FTIR-ATR). The FTIR-ATR spectra of tebuconazole indicate the presence of an –OH bond in the molecule through the medium intensity band in the region of 3291 cm^{-1} (Fig. 2A(a)).[27] They also present stretching of carbon bonds with the aromatic ring at 3137 cm^{-1} and symmetrical stretching related to methyl groups ($-CH_3$) in the band at 2975 cm^{-1}.[28] In the region of 1509 cm^{-1}, a characteristic vibration of the bond between the benzene ring and carbon bonds occurs.[27,29] The strong band evidenced at 1486 cm^{-1} corresponds to the vibration of the carbons present in the aromatic ring by the 'skeletal vibration' phenomenon.[29] The 2940 cm^{-1} band, in Fig. 2A-(e) and (f), presents the intensity and shape characteristic of the 2975 cm^{-1} band observed in the spectrum of pure tebuconazole. This suggests confirmation of the presence of the active substance in the dried coating films with the incorporation of the fungicide. The triadimenol spectra in Fig. 2B-(a) show a band of strong intensity at 3315 cm^{-1}, characteristic of the cyclic nitrogen present in the composition of the molecule. In the region of 2959 cm^{-1}, a band of medium intensity shows the presence of aliphatic carbons. Triadimenol, like tebuconazole, is a fungicide of the triazole class, characterized by the presence of cyclic bonds composed of nitrogen atoms, therefore presenting intense bands in the region between 1500 and 500 cm^{-1}, among them, the band at 1489 cm^{-1} is attributed to the asymmetric vibrations of the ring.[30] Since it is an aromatic ether, a band of strong intensity is evident at 1232 cm^{-1} and another at 1015 cm^{-1}, characteristic of the presence of C–O bonds in ethers.[31] Because the two substitutions in the aromatic ring are in the para position, a band of strong intensity is also observed at 823 cm^{-1}.[29–31]

In the FTIR-ATR spectra of LAPONITE® RD, presented in Fig. 2A-(b) and B-(b), a low-intensity absorption band at 3675 cm^{-1} is observed, characteristic of stretching vibrations of hydroxyl groups bonded to magnesium atoms. The bands located at 3438 cm^{-1} and 1641 cm^{-1} correspond to the stretching vibrations of the hydroxyl groups (OH–) present in the water molecules adsorbed by the clay. A high-intensity band evidenced at 960 cm^{-1} corresponds to the stretching vibrations of the Si–O bonds in the molecule and the presence of Si–O–Mg and Si–O–Si bonds throughout the structure. In the spectra of the CMC biopolymer, in Fig. 2A-(c) and B-(c), a strong intensity band at 3416 cm^{-1} indicates stretching vibrations of the –OH groups and intra and intermolecular hydrogen bonds.[20] The low intensity band at 2920 cm^{-1} indicates C–H bonds,[32,33] and the intensity band in

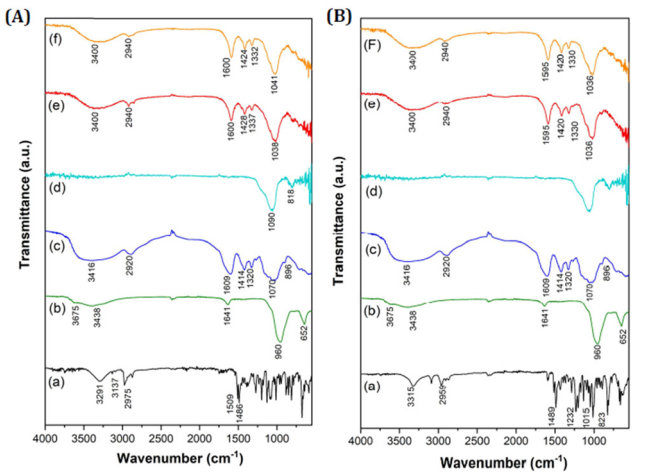

Fig. 2 FTIR-ATR spectra of: (A) – (a) TB P.A.; (b) LAP P.A.; (c) CMC P.A.; (d) SiO_2 NPs P.A.; (e) BTE coating; (f) CS5-TE coating. (B) – (a) TD P.A.; (b) LAP. P.A.; (c) CMC P.A.; (d) SiO_2 NPs P.A.; (e) BTR coating; (f) CS5-TR coating.

the 1609 cm^{-1} region occurs due to the presence of sodium carboxylate ($COO–Na^{+}$) groups in the molecule.[34] The broad band of medium intensity in the 1070 cm^{-1} region is characterized by the bond between C–OH, and at 896 cm^{-1}, by carbon–hydrogen bonds.[35] In the spectra of Fig. 2A-(e), (f) and B-(e) and (f), the characteristic bands of the CMC biopolymer present slight shifts, but confirm the presence in the synthesized organic–inorganic hybrid materials, by the bands 3400 cm^{-1}, 2940 cm^{-1}, 1600 cm^{-1}, and in the regions close to 1420 cm^{-1}, 1320 cm^{-1}, and 1040 cm^{-1}. The SiO_2 NPs, as shown in the spectra of Fig. 2A-(d) and B-(d), exhibit the characteristic peaks of the Si–O–Si bonds described in the literature, specifically in the low and strong intensity bands at 818 cm^{-1} and 1090 cm^{-1}, respectively.[36] In the dried coating films (Fig. 2A-(e), (f) and B-(e), (f)) an overlap of several bands is observed, such as the characteristic band of clay at 960 cm^{-1}, of SiO_2 NPs at 1090 cm^{-1} and of the biopolymer at 1070 cm^{-1}. The overlap of these three vibrational bands in the spectra of the dry coating films in the region near 1040 cm^{-1} and slight band shifts suggest interactions between the components. These interactions may reduce the crystallinity of the fungicide and promote better molecular dispersion, which may be associated with a more homogeneous distribution of the active ingredient, although this has not been directly measured.

3.3.3 Vibrational Raman spectroscopy analysis. The fungicide tebuconazole P.A. (Fig. 3A-(a)) is evidenced by the presence of several bands in the region between 1600 cm^{-1} and 640 cm^{-1}.[28] In the spectra presented here, a band of strong intensity is observed at 1598 cm^{-1}, characteristic of the group of triazoles, heterocyclic compounds formed by the presence of three nitrogen atoms in the same cyclic nucleus.[37] This band at 1598 cm^{-1} refers to the stretching vibrations of the C–C bonds of the disubstituted benzene ring.[38] Another band of strong intensity is observed in the region of 640 cm^{-1}, suggesting CCl stretching vibrations in the structure. Other medium-intensity peaks are also observed, such as stretching vibrations between CC and CO, evidenced at 1131.9 cm^{-1}.[39] Vibrations below 1000 cm^{-1} second refer to the skeletal structure of the active molecule, evidenced by intense peaks at 827 cm^{-1} and 640 cm^{-1}.[38] Two other intense bands at 1200 cm^{-1} and 1090 cm^{-1} refer to stretching vibrations, the first referring to carbons 1, 2, and 4 of the triazole ring and the second to the CO and CC bonds. The Raman spectra of LAPONITE® RD (Fig. 3A-(b) and B-(b)) show a band of strong intensity characteristic of the compound present at 684 cm^{-1}, referring to the symmetrical vibrations of SiO_4 in the structure of the clay layers.[40] In addition, the Raman spectrum of LAPONITE® RD can be grouped into two main regions: the stretching of the hydroxyl groups, between the region of 3750 cm^{-1} to 3550 cm^{-1}, and the region between 150 cm^{-1} and 1200 cm^{-1}, a region that highlights the functional groups present in the layers.[41] In the Raman spectra of the biopolymer sodium carboxymethyl cellulose (CMC), presented in Fig. 3A-(c) and B-(c), intense overlapping bands are observed in the region of the 2908 cm^{-1} peak attributed to stretching vibrations of the CH–CH_2 bonds and oscillations of the hydroxyl groups.[42] The triazole fungicides present characteristic bands of the ether functional group

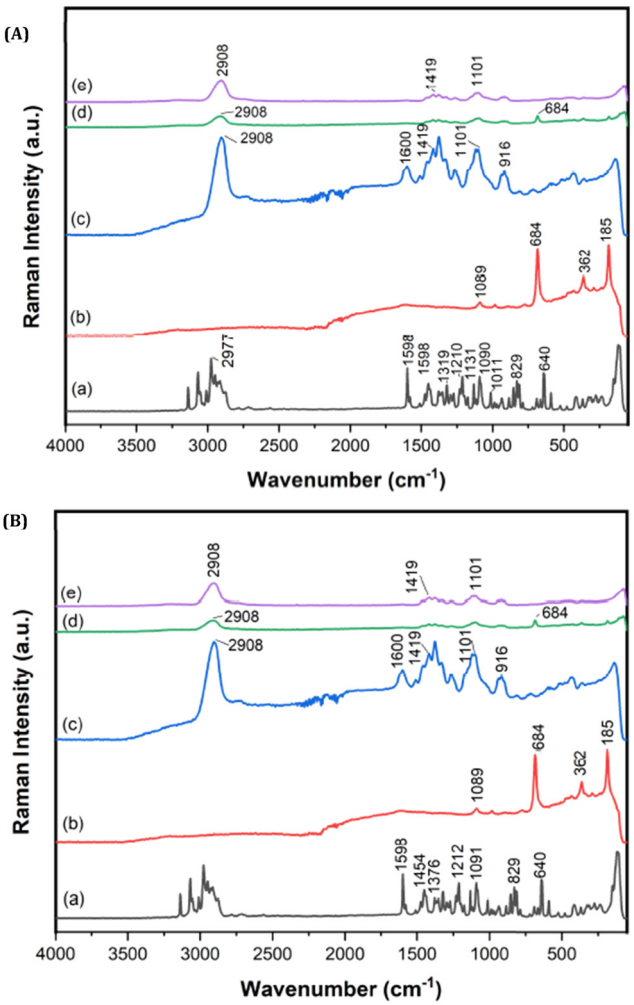

Fig. 3 Raman spectra of: (A) – (a) TB P.A.; (b) LAP P.A.; (c) CMC P.A.; (d) BTE coating; (e) CS5-TE coating; (B) – (a) TD P.A.; (b) LAP P.A.; (c) CMC P.A.; (d) BTR coating; (e) CS5-TR coating.

present in the aromatic ring of the structure in the region between 1200 and 1300 cm^{-1}, such as the band 1212 cm^{-1}. Other characteristic bands of the active ingredient are present in the region of 829 cm^{-1} and refer to the stretching vibrations of the C–O type and deformation vibrations of the C–C plane in the aromatic ring, and in the region of 640 cm^{-1}, which indicate torsion vibrational modes in the C–N bonds.[43] Observing the spectra in Fig. 3A-(d) and B-(d), of the BTE and BTR dried coatings films, respectively, it can be seen that the band at 684 cm^{-1} is present, even if with lower intensity, confirming the presence of LAPONITE® RD clay. The same occurs with the band at 2908 cm^{-1}, which validates the presence of the CMC biopolymer.[44] However, in the spectra of Fig. 3A-(e) and B-(e), of the CS5-TE and CS5-TR dried coatings films, which have SiO_2 NPs in their composition, the amorphization of the material did not reveal the band at 684 cm^{-1}, characteristic of the LAPONITE® RD clay, nor did it present the bands suggestive of the presence of the expected Si–O bonds, at 460 cm^{-1}, 800 cm^{-1} and 1070 cm^{-1}.

The Raman results of the dried coating films were interpreted comparatively, with emphasis on the persistence or

disappearance of the characteristic signals of LAPONITE® RD, CMC, triazole fungicides, and SiO_2. This comparative approach made it possible to identify spectral differences between BTR, BTE, CS5-TR, and CS5-TE as a consequence of the reorganization of the hybrid network, the altered coating morphology, and the distinct antifungal performance of the silica-containing formulations.

3.3.4 Thermogravimetric analysis and differential scanning calorimetry (TG, DTG, and DSC). The thermograms in Fig. S1(A) and (C) in the SI show a pattern in the mass loss of the BTE and BTR samples, which may be related to their similar coating compositions, since both contain triazole precursors, LAPONITE® RD clay, and carboxymethylcellulose biopolymer. Both show mass decomposition of approximately 35% between 200 and 400 °C, which may be associated with the loss of water linked to the organic–inorganic hybrid material. Furthermore, a gradual loss of mass is observed until the end of the analysis at 600 °C, which must be a result of the elimination of water from the inorganic part originating from the LAPONITE® RD clay.[45] Observing the differential scanning calorimetry (DSC) thermograms of the BTE and BTR dried coating films (Fig. S1(B) and (D)), we find an exothermic event in the range of 250–260 °C, followed by an endothermic event in the temperature range of 260–280 °C, which suggests two thermal events: crystallization and melting, respectively. Additionally, an upward trend is observed in the DSC curves until the end of the analysis, at 300 °C, which suggests an ongoing oxidation event. Both dried coating films exhibit a glass transition at the beginning of the DSC curve, with an endothermic character around 75 °C and an exothermic crystalline transition around 278 °C, as described in the literature for polymeric materials containing CMC in their composition.[46]

Observing the thermograms in Fig. S1(E) and (G) of the CS5-TE and CS5-TR samples, a mass loss pattern of approximately 40% is observed between 250 and 300 °C, a loss suggestive of water bound to the hybrid material. In addition, the CS5-TE sample exhibits a more significant mass loss from 300 °C, reaching approximately 30% of the total initial mass. Similarly, the CS5-TR sample reaches approximately 40% of the total mass at the end of the analysis. This suggests greater water retention by the CS5-TE and CS5-TR dried coating films compared to dried coatings film without the presence of SiO_2 NPs. This increased water retention may result from the high surface area and hydrophilic nature of the SiO_2 NPs present in the coatings.[47] This behavior is consistent with the formation of more hydrated networks, which may play a crucial role in swelling and act as a carrier system by coating the matrix.

Observing the differential scanning calorimetry (DSC) thermograms of the CS5-TE and CS5-TR samples in Fig. S1(F) and (H), we note a broad glass transition with a *Tg* of around 60 °C, indicating an exothermic event in the range of 250–260 °C, followed by an endothermic event in the range of 260–280 °C, which suggests the thermal events of crystallization and melting, respectively. Furthermore, an upward trend is observed in the DSC curves until the end of the analysis, in the CS5-TE sample, at 300 °C, which suggests an ongoing oxidation event. The same does not occur for sample CS5-TR, which shows a downward curve at the end of the analysis, at 300 °C, characteristic of the thermal decomposition event.

3.3.5 Scanning electron microscopy (SEM) and energy dispersive X-ray spectroscopy (EDS) analysis. Fig. 4 shows top-plane images of the BTR, BTE, CS5-TR, and CS5-TE dried coating films. Fig. 4(A) shows the CS5-TR coating viewed from above at a magnification of 2.5×10^3. The coating surface has a rough texture, justified by the presence of incorporated nanoparticles. The elemental map obtained by the EDS technique, shown in Fig. 5A-(a), confirmed the predominance of the element silicon

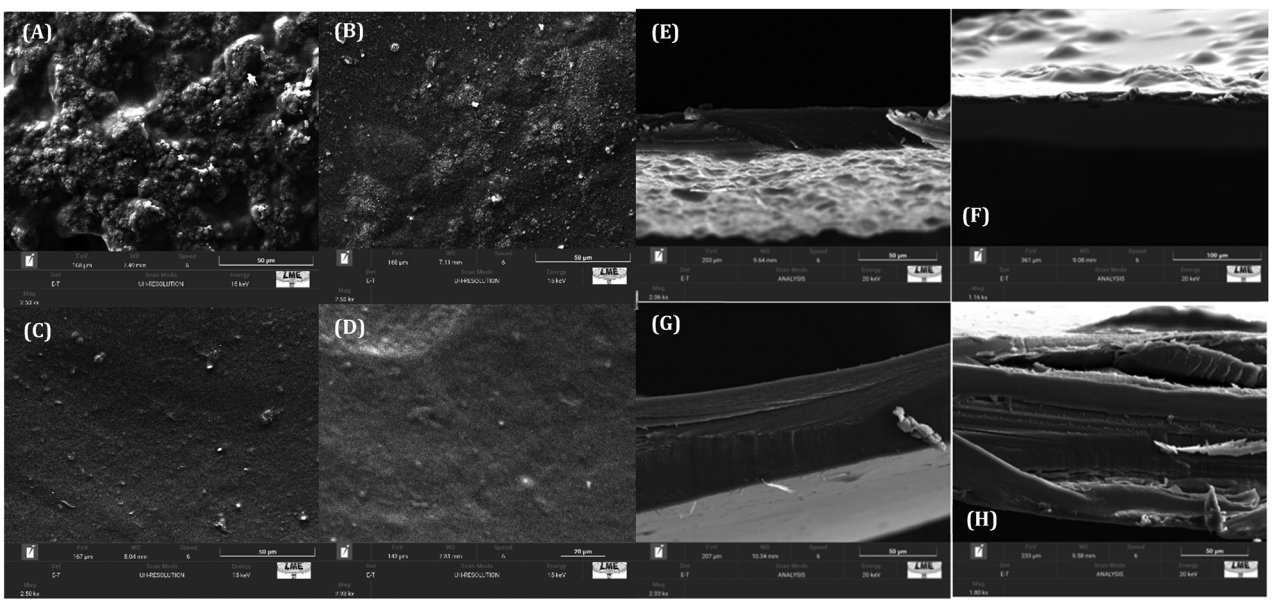

Fig. 4 Scanning electron microscopy (SEM) images top plane at a magnification of 2.5×10^3 in: (A) CS5-TR; (B) CS5-TE; (C) BTE; (D) BTR; and cross-sections of the coating in: (E) CS5-TR; (F) CS5-TE; (G) BTE; (H) BTR.

on the coating surface, in addition to the presence of oxygen, sodium, and aluminum, respectively, in smaller concentrations. This suggests that the SiO_2 NPs were concentrated on the surface during the material drying process. The CS5-TR dried coating films had an average thickness of 24.7 μm, forming thinner and more malleable layers than those observed in dried coating films without SiO_2 NPs in their composition.

Fig. 4B shows the CS5-TE dried coating films viewed from above, also at a magnification of 2.5×10^3. The presence of SiO_2 NPs in the coating was also confirmed by elemental map analysis, showing silicon, sodium, and oxygen in the composition. As with the CS5-TR dried coating films, a more homogeneous surface was observed, characterized by the fixation of silicon in the surface area. The thickness of the CS5-TE dried coating films was 18.9 μm, the smallest observed among the measured samples. The low thickness of the dried coating films, with the presence of SiO_2 NPs, is consistent with the suspensions obtained in the syntheses, which have low viscosity. As discussed in the diffractograms presented by the CS5-TR and CS5-TE dried coating films, the disappearance of the characteristic peak of the LAPONITE® RD clay suggests a modification in the intercalation of the clay in the presence of silicon, which implies a change in the texture, viscosity, and thickness of the material. The enhanced antifungal performance observed for the CS5-TR and CS5-TE dried coating films may be associated with the structural and morphological features of the hybrid coatings. The SEM–EDS elemental maps indicate localized silicon enrichment at the coating surface, while the cross-sectional images show thinner and more flexible dried coating films for the SiO_2-containing systems. This surface-localized silicon enrichment is discussed as a structural feature associated with the distinct behavior of the silica-containing coatings, rather than only as an elemental mapping observation. Together with the structural changes inferred from XRD, these observations suggest that silica incorporation may modify the organization of the hybrid matrix and may favor a more effective coating–fungus interaction and local availability of the triazole fungicides. Fig. 4C shows images of the BTE coating at 2.5×10^3 magnification. The coating has a thickness of 285.52 μm, the thickest among those measured. In addition to being thicker, the material was less malleable and more brittle than those containing silicon. The same occurs in Fig. 4D, which shows images of the BTR dried coatings films at the same magnification of 2.5×10^3. The coating has an average thickness of 139.96 μm and also exhibits a lamellar and brittle nature. The cross-sectional images of the BTE and BTR dried coating films, in Fig. 4G and H, indicate the formation of sieves, suggesting a lamellar structure, *i.e.*, in layers, typical of the presence of larger tactoids with basic structural units stacked parallel to each other.[48] Furthermore, the average thicknesses of the BTE and BTR dried coating films suggest a distinct organization of the LAPONITE® RD clay particles, with the tactoids grouped in stacked layers.[49] The reduction in coating thickness observed for CS5-TR and CS5-TE (18–25 μm) in Fig. 4E and F compared with BTR and BTE dried coating films (>130 μm) indicates that the incorporation of SiO_2 NPs is associated with substantial changes in the organization of the hybrid polymer–clay network. In combination with the XRD and Raman results, this behavior is consistent with the disruption of the original clay stacking/interlayer organization and with the formation of thinner and more flexible dried coating films. These structural and morphological differences may help explain why the silica-containing coatings exhibited superior antifungal performance.

Furthermore, the significant reduction in the thickness of SiO_2-containing coatings may contribute to greater local availability of the active ingredients and to a more effective coating–fungus interaction. Additionally, the preferential location of

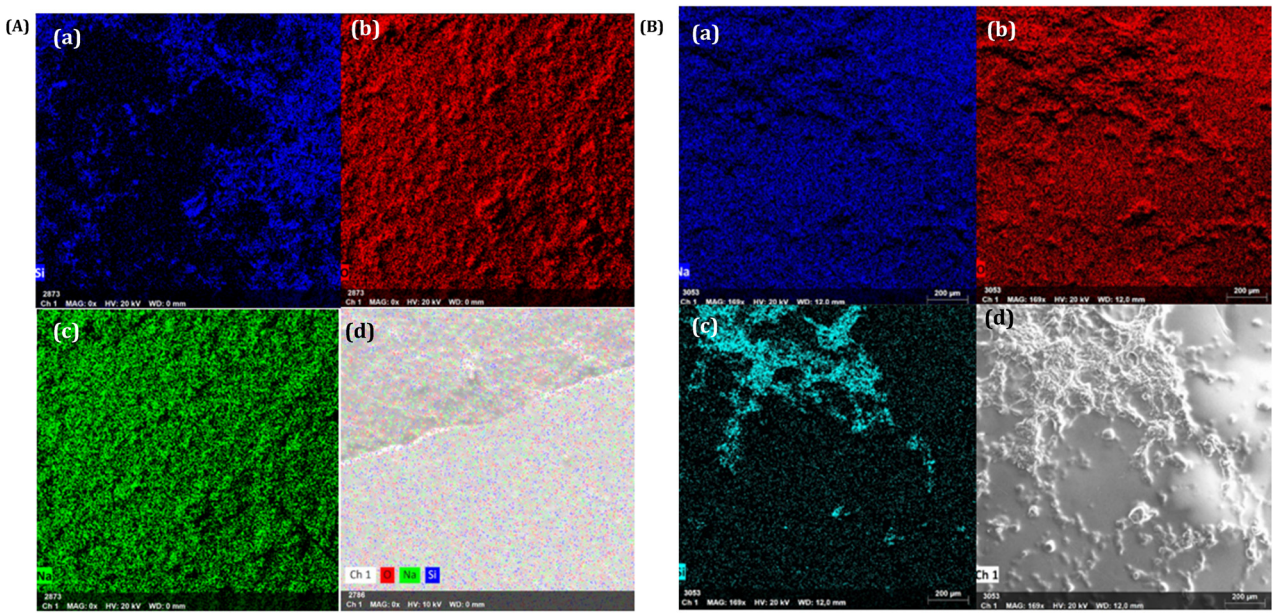

Fig. 5 (A) Images of the elemental maps obtained for sample CS5-TR showing: (a) silicon, (b) oxygen, (c) sodium, and (d) hydrocarbons, oxygen, sodium, and silicon. (B) Images of the elemental maps obtained for sample CS5-TE showing: (a) sodium, (b) oxygen, (c) silicon, and (d) hydrocarbons.

SiO_2 NPs on the coating surface can modulate local microenvironmental conditions unfavorable to fungal growth.

Fig. 5A and B show the images of the elemental maps obtained for samples CS5-TR and CS5-TE, respectively. In both groups of images, there is homogeneity in the distribution of the elements oxygen and sodium in the coating structure. Sodium is found in the interlamellar galleries of the LAPONITE® RD clay and disperses in the aqueous medium, dissociating and promoting a negative charge on the disks, while oxygen, present in the composition of the carboxymethyl cellulose polymer, is also found in the positively charged hydrated magnesium and silica oxides on the edges of the clay and in the silicon dioxide incorporated into the coating.[50] The silicon present in both dried coating films, originating from the silica bound to the clay oxides and to the SiO_2 NPs incorporated in the synthesis, is distributed heterogeneously over the analyzed area (Fig. 5A-(a) and B-(c)). The agglomerated distribution of the silicon element suggests that particles in the form of silicon dioxide, which naturally form these aggregated structures.[51] This is confirmed by the distribution of the silicon element in the BTE and BTR dried coating films, indicating no incorporation of SiO_2 during synthesis.

Therefore, the elemental maps show a homogeneous distribution of the element in the analyzed area (Fig. S2 (a) and (b)), with 35.76% and 21.26%, respectively, being the mass percentages in the analyzed regions.

The paired comparison between the triazole-containing coatings without SiO_2 (BTR and BTE) and their corresponding SiO_2-containing formulations (CS5-TR and CS5-TE) shows that silica incorporation was associated with a marked increase in mycelial growth inhibition against *S. cepivora*. This enhanced response may be associated with the structural and morphological features of the hybrid coatings, including reduced thickness and greater flexibility, localized silicon enrichment at the coating surface, and reorganization of the polymer–clay network. Together, these characteristics may favor more effective contact between the coating and fungal structures and improve the local availability of the triazole fungicides.

The EDS results confirmed the presence of oxygen as the chemical element with the highest concentration. In the coatings with the incorporation of SiO_2 NPs in the synthesis, the sodium element was the second in mass percentage, followed by silicon. In the coatings without the presence of SiO_2 NPs in the synthesis, silicon was the second element in mass percentage, followed by the elements sodium, manganese, and fluorine. The absence of fluorine and manganese in the coatings with SiO_2 incorporation suggests a greater affinity between silicon and the interlamellar region.

4. Conclusions

The incorporation of SiO_2 NPs into hybrid coatings containing the fungicides triadimenol and tebuconazole induced total inhibition of *S. cepivora* mycelial growth. Furthermore, there is a structural reorganization in the coatings containing SiO_2 NPs, fungicides, and the precursors used in the synthesis of the hybrid coatings, suggesting an interaction between the components of the coatings. In the XRD diffractograms and in the FTIR-ATR and Raman spectra, there was a decrease and disappearance of signals, as well as shifts, also suggesting active polymer–clay, clay–silica, and membrane–fungicide interactions. Regarding the fungicides used, the low incorporation concentrations in the coatings did not indicate their presence in the analyzed diffractograms and spectra. However, low concentrations of fungicides did not prevent their inhibitory effect on the mycelial growth of *S. cepivora*, especially when evaluated in coatings with SiO_2 NPs, preventing the appearance of symptoms in both mycelial growth inhibition (ICM) tests performed on onion seeds (*Allium cepa* L.) and on dry coatings. The thermal analysis of the hybrid coatings allowed us to verify the thermal stability of the coatings, highlighting the main decomposition event in the range of 200 to 400 °C, justified by the dehydration of the molecules. The results of this study highlight the potential of hybrid coatings containing SiO_2 for antifungal applications. In addition, the characterization techniques used indicated structural and morphological changes in the coating matrix after the incorporation of SiO_2. Future studies should include release kinetics, coating permeability, seedling infection assays, and validation under soil conditions to investigate the behavior of this pretreatment in crops affected by *S. cepivora*. The study of fungicide and SiO_2 NP concentrations may also allow for the management of *S. cepivora*, considering its use in hybrid coatings and seed immersion, which would have a positive impact on reducing production costs and reducing the volume of commercial fungicides used in crops attacked by the fungus.

Author contributions

Lorena Alves de Melo Bessa: conceptualization, investigation, data curation, methodology, and writing the original draft. Jairo Tronto: resources, investigation and supervision and review and editing. Franciely Junia Alves de Camargos: investigation and project contributions. Amanda M. Oliveira: investigation and project contributions. Celly Mieko Shinohara Izumi: review and editing. Everaldo Antônio Lopes: review and editing. Eduardo Alves: review and editing. Eduardo Seiti Gomide Mizubuti: review and editing.

Conflicts of interest

The authors declare no competing interests.

Data availability

All data supporting the findings of this study—including planting data and statistical analyses—are fully provided within the published article and its supplementary information (SI). No additional datasets have been generated or deposited in external repositories. Supplementary information is available. See DOI: https://doi.org/10.1039/d5ma01038a.

Acknowledgements

Lorena Alves de Melo Bessa gratefully acknowledges the Coordenação de Aperfeiçoamento de Pessoal de Nível Superior – CAPES (Process Number: 88887.678485/2022-00). Dr Tronto thanks Fundação de Amparo à Pesquisa de Minas Gerais – FAPEMIG (Process Numbers: APQ-03410-22 and RED-00056-23) and Conselho Nacional de Desenvolvimento Científico e Tecnológico – CNPq (Process Number: 302591/2023-0). The authors are grateful to the Federal University of Juiz de Fora and the Federal University of São Paulo for providing different characterization techniques used in this study. Dr Tronto and Lorena Alves de Melo Bessa gratefully acknowledge the Federal University of Viçosa, Rede Mineira de Química (RQ-MG), and the Programa de Pós-Graduação Multicêntrico em Química de Minas Gerais (PPGMQ-MG) for the structure and support in the research.

Notes and references

1 M. Faustini, *et al.*, *Adv. Funct. Mater.*, 2018, **28**(27), 30.
2 K. S. Lima, *et al.*, *Res. Soc. Dev.*, 2021, **10**, 13.
3 A. Shelar, S. H. Nile, A. V. Singh, D. Rothenstein, J. Bill, J. Xiao, M. Chaskar, G. Kai and R. Patil, *Nano-Micro Lett.*, 2023, **15**, 54, DOI: 10.1007/s40820-023-01025-5.
4 T. Javed, I. Afzal, R. Shabbir, K. Ikram, M. S. Zaheer, M. Faheem, H. H. Ali and J. Iqbal, *J. Saudi Soc. Agric. Sci.*, 2022, **21**, 536–545, DOI: 10.1016/j.jssas.2022.03.003.
5 M. Gallo, *et al.*, *Int. J. Mol. Sci.*, 2024, **25**(2), 1108.
6 D. R. Caroline Nunes, *et al.*, *ACS Omega*, 2026, **11**(4), 6671–6682.
7 J. H. S. Soares, *et al.*, *ACS Agric. Sci. Technol.*, 2025, **5**(2), 142–157.
8 P. Goswami, J. Mathur and N. Srivastava, *Heliyon*, 2022, **8**, e09908, DOI: 10.1016/j.heliyon.2022.e09908.
9 A. M. Elenany, *et al.*, *Biology*, 2024, **13**(4), 219.
10 D. M. B. Lorena Alves, *et al.*, *Dalton Trans.*, 2024, **53**(18), 7880–7889.
11 Y. Liang, C. Fan, H. Dong, W. Zhang, G. Tang, J. Yang, N. Jiang and Y. Cao, *ACS Sustainable Chem. Eng.*, 2018, **6**, 10211–10220, DOI: 10.1021/acssuschemeng.8b01511.
12 Y. Gao, Y. Liang, H. Dong, J. Niu, J. Tang, J. Yang, G. Tang, Z. Zhou, R. Tang, X. Shi and Y. Cao, *ACS Sustainable Chem. Eng.*, 2020, **8**, 5716–5723, DOI: 10.1021/acssuschemeng.0c00649.
13 T. M. Abdelrahman, X. Qin, D. Li, I. A. Senosy, M. Mmby, H. Wan, J. Li and S. He, *Chem. Eng. J.*, 2021, **404**, 126440, DOI: 10.1016/j.cej.2020.126440.
14 P. Zhao, C. Wang, S. Zhang, L. Zheng, F. Li, C. Cao, L. Cao and Q. Huang, *J. Hazard. Mater.*, 2022, **425**, 127892, DOI: 10.1016/j.jhazmat.2021.127892.
15 A. M. Shershneva, *et al.*, *J. Environ. Sci. Health, Part B*, 2019, **54**(3), 196–204.
16 M. C. Pinto, *et al.*, *Microporous Mesoporous Mater.*, 2016, **225**, 342–354.
17 V. de and A. M. Gonzaga, *et al.*, *J. Biomed. Mater. Res., Part B*, 2020, **108**(4), 1388–1397.
18 C. D. Cordella, *et al.*, *J. Appl. Polym. Sci.*, 2003, **87**(13), 2074–2079.
19 D. F. Burgardt, *et al.*, *J. Food Nutr. Res.*, 2012, **51**, 4.
20 R. Lin, *et al.*, *Carbohydr. Polym.*, 2015, **118**, 126–132.
21 P. H. De Miranda, *et al.*, *Sugar Tech.*, 2026, 1–12, DOI: 10.1007/s12355-026-01730-6.
22 X. Cai, *et al.*, *Constr. Build. Mater.*, 2016, **127**, 804–814.
23 P. Sheoran, *AIP Conf. Proc.*, 2020, **2270**, 10042.
24 D. S. Dos Santos and D. R. Dos Santos, *J. Non-Cryst. Solids*, 2002, **304**(1–3), 56–63.
25 C. M. Poffo, *et al.*, *Phys. B*, 2012, **407**(24), 4686–4694.
26 V. A. M. Gonzaga, *et al.*, *J. Biomed. Mater. Res., Part B*, 2020, **108**(4), 1388–1397.
27 O. Anjos, *et al.*, *Food Chem.*, 2015, **169**, 218–223.
28 R. P. Cordeiro, *et al.*, *Aquacult. Res.*, 2022, **53**(4), 1446–1455.
29 K. Qian, *et al.*, *Microporous Mesoporous Mater.*, 2013, **169**, 1–6.
30 R. Ameta and C. Suresh, *Photocatalysis: principles and applications*, CRC Press, 2016.
31 H. Tomás, *et al.*, *Nanomedicine*, 2018, **14**(7), 2407–2420.
32 K. M. Tavares, *et al.*, *Carbohydr. Polym.*, 2020, **246**, 116521.
33 Q. Xiao, L. Lim and Q. Tong, *Carbohydr. Polym.*, 2012, **87**(1), 227–234.
34 C. Wu, *et al.*, *J. Agric. Food Chem.*, 2002, **50**(2), 378–383.
35 V. C. D. F. Burgardt, *et al.*, *J. Food Nutr. Res.*, 2012, **51**, 4.
36 R. Ahlawat, *et al.*, *J. Alloys Compd.*, 2024, **995**, 174858.
37 M. R. Reis, *et al.*, *Pesqui. Agropecu. Trop.*, 2011, **41**, 587–594.
38 Z. Jurašeková, *et al.*, *Spectrochim. Acta, Part A*, 2022, **268**, 120629.
39 J. Li, *et al.*, *J. Food Compos. Anal.*, 2024, **133**, 106380.
40 N. Iturrioz-Rodriguez, *et al.*, *Appl. Surf. Sci.*, 2021, **537**, 10.
41 J. T. Kloprogge, *Dev. Clay Sci.*, 2017, **8**, 150–199.
42 B. Rojek, *et al.*, *Spectrochim. Acta, Part A*, 2023, **302**, 123048.
43 B. N. Da Silva, *et al.*, *Vib. Spectrosc.*, 2023, **129**, 103606.
44 M. M. Campos-Vallette, *et al.*, *J. Raman Spectrosc.*, 2010, **41**(7), 758–763.
45 P. A. Wheeler, J. Wang and L. J. Mathias, *Chem. Mater.*, 2006, **18**(17), 3937–3945.
46 S. El-Sayed, *et al.*, *Phys. B*, 2011, **406**(21), 4068–4076.
47 M. Fernandez-Garcia, *et al.*, *Chem. Rev.*, 2004, **104**(9), 4063–4104.
48 H. Pálková, *et al.*, *Microporous Mesoporous Mater.*, 2010, **127**(3), 228–236.
49 P. Au, *et al.*, *Chem. Eng. Res. Des.*, 2015, **101**, 65–73.
50 S. Jatav and Y. M. Joshi, *Appl. Clay Sci.*, 2014, **97**, 72–77.
51 M. H. Khan, *et al.*, *Constr. Build. Mater.*, 2024, **419**, 135483.